ACS Catalysis

pubs.acs.org/acscatalysis

Research Article

Ripening of Rh Nanoparticle Catalysts in Reverse Water–Gas Shift via a Data-Driven Model Combining Physics, Theory, and Experiment

Natalie M. Isenberg,*,⊥ Yonghyuk Lee,⊥ Carolina Colombo Tedesco, Zhihengyu Chen, Anastassia N. Alexandrova, Christopher J. Tassone, Robert Rallo, and Simon R. Bare

Cite This: *ACS Catal.* 2026, 16, 10398–10410

Read Online

ACCESS | Metrics & More | Article Recommendations | Supporting Information

ABSTRACT: Degradation via sintering is an ongoing challenge that impedes the broad commercial success of supported metallic nanoparticle catalysts. To mitigate degradation via informed catalyst design and process operations, here we aim to disambiguate the underlying mechanisms of sintering by combining theory and experiment in a quantitative framework. While mechanistic sintering models exist, they only model a single sintering pathway, even though multiple sintering mechanisms can occur simultaneously or dominate at different stages of the process. Data-driven machine learning models have emerged as a means to represent complex processes through data regression. However, machine learning models have very large data needs and lack mechanistic insights due to their black-box encoding. To develop an interpretive model of catalyst degradation via sintering, we constructed a *hybrid model* combining mechanistic "physics-based" models and data-driven methods to obtain both reliable predictions and mechanistic insights regarding experimentally observed sintering phenomena. Focusing on nanoparticle sintering in the Rh–TiO_2 catalyst for the reverse water–gas shift (RWGS) reaction, the hybrid model couples a mechanistic term for Ostwald ripening with energy values calculated via density functional theory (DFT) with a parametric, data-driven discrepancy function term for unmodeled mechanisms. The hybrid model is trained using Bayesian inference with data collected from small-angle X-ray scattering (SAXS) in situ experiments wherein average nanoparticle diameter versus time was measured at three relevant operating temperatures. The calibrated hybrid model results show that an Ostwald ripening-only model parameterized with fixed DFT energies does not fully capture the time and temperature dependence of the SAXS-observed sintering kinetics, and that an additional functional contribution, or DFT energy calibration, is required to reconcile simulation and experiment. Analysis of the hybrid-model error confirms that the hybrid model outperforms both the purely mechanistic and purely data-driven alternatives in terms of expected predictive accuracy for time-evolving average particle sizes. Furthermore, the results support the hypothesis that the Ostwald ripening mechanism is less important for explaining the sintering phenomena as operating temperature increases under an assumed fixed DFT parameterization. This could be explained in one of two ways: either latent, unmodeled sintering mechanisms dominate at higher temperatures, or the DFT uncertainty increases with temperature. The proposed modeling approach directly links theory to experiments and simulations via a statistical hybrid modeling framework and can be extended to other catalytic systems to improve predictive models and mechanistic understanding.

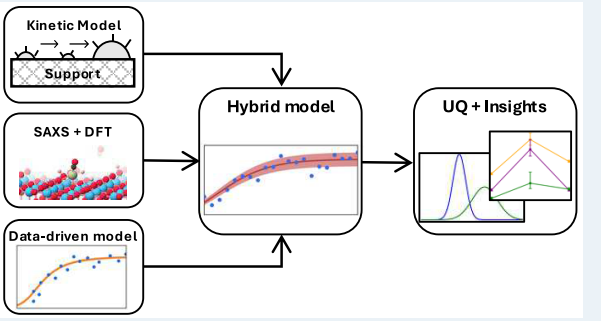

KEYWORDS: *catalyst sintering, Bayesian hybrid modeling, multi-modal data*

1. INTRODUCTION

Supported metallic catalysts play a central role in enabling energy-efficient chemical processes. However, degradation caused by the reduction in the surface-area-to-volume ratio of supported metallic nanoparticle catalysts under reactive process conditions remains a fundamental challenge in industrial applications.[1] For the purposes of this study, we focus on a specific system of Rh–TiO_2 catalysts under relevant operating conditions for the reverse water–gas shift (RWGS) reaction. While supported Rh nanoparticles are catalysts of interest for the RWGS reaction, their industrial application has been limited due to high relative costs.[2,3] Studies have shown that smaller, well-dispersed nanoparticles are ideal for decreasing metal costs and ensuring selectivity of the RWGS reaction toward the desired products.[4,5] Therefore, there is a need to understand and mitigate degradation in these catalysts through informed

Received: February 24, 2026
Revised: April 29, 2026
Accepted: May 1, 2026
Published: May 21, 2026

catalyst design and process operations. Among the different mechanisms for nanoparticle catalyst degradation, we focus on sintering (i.e., ripening), which can occur by Ostwald ripening[6,7] and Smoluchowski ripening (i.e., diffusion/coalescence).[8] Ostwald ripening is a process by which metal atoms form monomers and diffuse across the surface to larger particles. Smoluchowski ripening is a process where entire particles migrate across the surface to combine into larger particles. Under certain reaction conditions (e.g., high temperature and high reactant partial pressures), there is also the potential for disintegration and re-dispersion.[9] Disintegration is facilitated by reactants redistributing supported metal particles into complexes spread across the support.

Kinetic and empirical models exist for the aforementioned mechanisms.[6,8,10] While these models are useful for predicting the time evolution of catalyst sintering in a first-principles, physics-based framework, there are also several shortcomings. First, first-principles models require physical parameter data, such as diffusion energies, which are challenging to obtain and are system-specific, limiting their general applicability. These models are considered "high-fidelity" in that they aim to most accurately describe the physics and chemistry of the underlying processes. However, in many cases, the computational complexity of solving these mechanistic models is too great, leading to simplifying assumptions. Furthermore, each of these kinetic models captures only one mechanism. In reality, there may be multiple sintering mechanisms occurring simultaneously or dominating at different regimes of the catalytic process.[11,12] Which sintering mechanisms are observed for a given process depends on the strength of the metal–metal and metal–support interactions and is generally challenging to disentangle from experimental data.[13] Understanding which of the sintering mechanisms are dominant, and to what extent they contribute to the deactivation of an industrial catalyst, is an important research question which we hope to make gains toward through this work.

Whereas kinetic and empirical models are based on first-principles knowledge, machine learning (ML), data-driven, or *black-box* models rely purely on data. In contrast to mechanistic models, which come from a physical understanding of a real process, data-driven models generally do not require any prior knowledge. These models are highly flexible and capable of predicting otherwise "unmodeled" phenomena through inference from data. In the area of catalysis, black-box ML models have been used to predict transition states,[14] compute interatomic potentials,[15,16] perform molecular dynamics simulations,[17] and even predict conversion rates over time in an industrial process.[18] However, these purely data-driven methods are not devoid of challenges. For example, black-box models are often data-intensive, requiring large amounts of high-quality data to make reliable predictions. Additionally, the high-dimensional regression parameter space of these nonlinear models is often uninterpretable and also prone to over-fitting. This means that while data-driven/black-box models can fit experimental or simulation data with high accuracy, there is little to no understanding obtained about the underlying model (or mechanism) itself.[19]

There has been increasing interest in the application of *hybrid* models, or *gray-box* models, for decision-making in science and engineering.[20,21] The advantage of these hybrid models is that they lie somewhere in the middle of the continuum of physical and black-box models. Hybrid models combine the important physics of mechanistic models with data-driven methods that can capture any unmodeled factors hidden in the data. These models have been applied to predict process performance in different industrial reactor settings. For example, Bui et al.[22] modeled an industrial reactor utilizing a heterogeneous catalyst under adiabatic conditions. Kay et al.[23] used a hybrid kinetic model with an artificial neural network to predict chemical reaction kinetics in an industrial water−gas shift reaction system. Jorner et al.[24] applied a hybrid modeling approach combining density functional theory with Gaussian process regression to improve predictions of reaction barriers. Finally, Luo et al.[25] developed a hybrid model for a packed fixed-bed reactor using a support vector machine regression model to represent unknown catalyst deactivation dynamics. Bayesian hybrid modeling approaches, which take a statistical perspective, were first proposed in work by Kennedy and O'Hagan [26] and have been successfully applied in an ever broader array of scientific and engineering settings, including carbon capture systems,[27,28] ice sheet modeling,[29] structural engineering,[30] pharmacodynamic models for drug design,[31] climate model sensitivity,[32] and decision-making under uncertainty.[33]

The present work aims to construct an interpretable Bayesian hybrid model of kinetic sintering phenomena for a population of supported Rh−TiO_2 nanoparticle catalysts under reactive RWGS conditions, as presented in Figure 1. We propose two main functional components to the hybrid model of sintering. First, as shown in Figure 1A,C, we include a first-principles, kinetic model of Ostwald ripening that simulates, under a given computed DFT energy parameterization, the average particle radius over time in a population of supported metallic nanoparticles under reaction conditions. Second, as shown in Figure 1D, we add data-driven parametric discrepancy functions devised with expert prior knowledge to model mechanistic sintering phenomena in Rh−TiO_2 not explained by Ostwald ripening, DFT energies, and noise alone. To fit the hybrid sintering model (Figure 1E), Bayesian inference (calibration) is carried out using experimental in situ small-angle X-ray scattering (SAXS) data of average Rh−TiO_2 nanoparticle spherical diameter (radius) over time (Figure 1B). Bayesian inference is used for calibration in this framework as it provides interpretability via implicit uncertainty estimates. In the setting of industrial catalyst design, interpretability is highly desirable because we do not wish to simply know *which conditions* (e.g., temperature, initial particle size) lead to a given deactivation behavior, but also *which mechanism(s)* are most likely leading to deactivation, given the conditions.

The proposal herein is to demonstrate that informed catalyst design can be accelerated with interpretable hybrid models for catalyst ripening via sintering. This hybrid modeling framework is generic and can be applied to the study of any mechanistic phenomena in catalyst systems. Overall, the hybrid modeling approach allows for meaningful interpretations wherein the relative importance of physically meaningful parameters and data-driven components can be quantified. This can facilitate greater insights into the underlying physical mechanisms driving nanoparticle sintering across experimental operating conditions and highlight the trade-offs between established physical models and phenomenological data-driven models.

2. METHODS

2.1. The Kinetic Model

The first model for the kinetics of supported catalyst sintering via Ostwald ripening (OR) was derived in a seminal paper by

https://doi.org/10.1021/acscatal.6c01516
ACS Catal. 2026, 16, 10398−10410

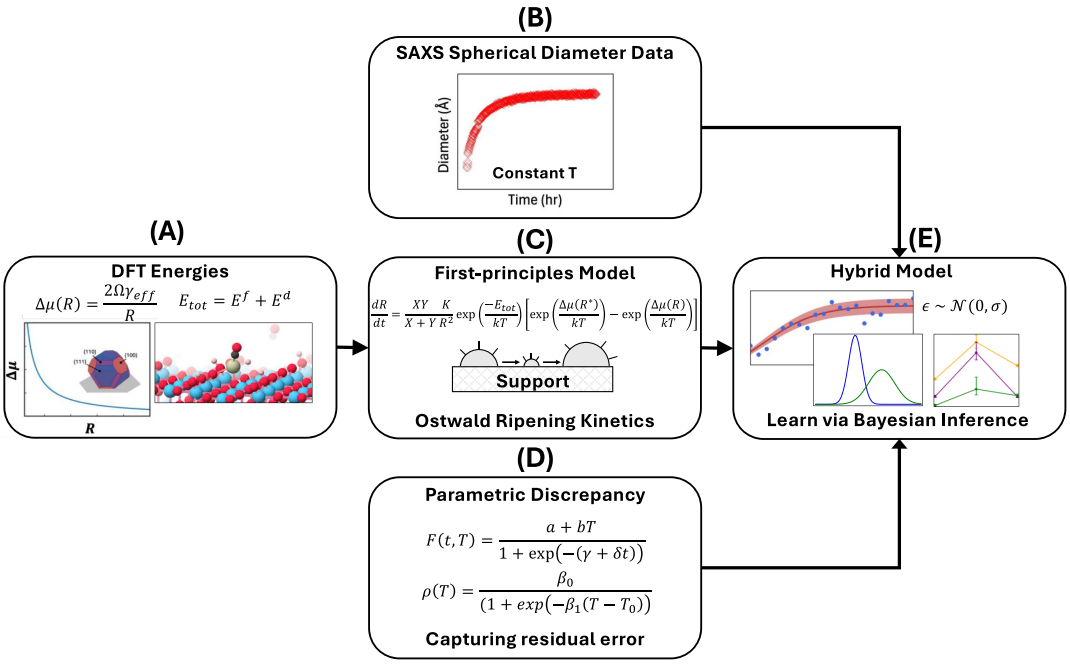

Figure 1. Schematic of the proposed hybrid modeling framework. (A) Energies for surface-bound Rh species are calculated via DFT at each reaction temperature to estimate E_{tot} values as well as a radius-dependent $\Delta\mu(R)$ for the Ostwald ripening kinetic model. (B) Spherical particle diameter over time computed using in situ SAXS measurements under reaction conditions provides an experimental dataset to calibrate the hybrid-model parameters. (C) First-principles Ostwald ripening kinetic model describes a single sintering mechanism via a dynamic system of nonlinear, coupled ordinary equations. (D) Parametric discrepancy functions are used to capture residual error between the Ostwald ripening kinetics under a fixed DFT energy parameterization. (E) Calibrated (trained) hybrid model provides time-series predictions of average nanoparticle catalyst radius evolution, confidence intervals, and the ability to study temperature-dependent mechanistic phenomena.

Wynblatt and Gjostein.[34] Parker and Campbell[35] built upon this work by including more accurate particle-size-dependent energetics. Later work by Ouyang et al.[6] extends upon these kinetic models further by developing a model for reactant-assisted Ostwald ripening. Because we are interested in developing a hybrid model for Rh−TiO_2 catalyst sintering in the RWGS reaction, we utilize the reactant-assisted kinetic model,[6] which is presented in eq 11.

$$\frac{dR}{dt} = \frac{XY}{X+YR^2}\frac{K}{R^2}\exp\left(\frac{-E_{tot}}{kT}\right)\left[\exp\left(\frac{\Delta\mu(R^*)}{kT}\right) - \exp\left(\frac{\Delta\mu(R)}{kT}\right)\right] \quad (1)$$

In this formulation, R is the nanoparticle radius, X, Y, and K are lumped parameters (see SI Section 4), $\Delta\mu$ is the chemical potential of the supported nanoparticle computed using the Gibbs−Thompson relation,[34] as shown in SI Section 4 eqs 8 and 9, R^* is the critical radius, and E_{tot} is the total activation energy. The critical radius is defined as the equilibrium nanoparticle size and is also the term which drives mass transfer between particles. In this model, any particles within the population that have a radius above R^* at any given time will grow in size, while particles below the critical radius will decrease in size.

In practice, the ordinary differential equation (ODE) in eq 1 is not for a single particle, but for a population of N nanoparticles, wherein each particles radius is a function of all other particle radii due to the dependence on the critical radius, R^*. This is because the critical radius is a function of all the radii R within the population of N particles, i.e., $R^*(R_1, \cdots, R_N)$. For computational simplicity, the method for computing critical radius is the harmonic average, as defined in Parker and Campbell.[35] Eq 2 shows the system of initial value ordinary differential equations for simulating the OR kinetics of a population of N nanoparticles with initial radii $R_i(0) = R_{i,0}$, $R_{i,0} \sim \mathcal{N}(\mu_0, \sigma_0^2)$, $\forall i \in [1, \cdots N]$, where μ_0 is the initial mean radius of the nanoparticle size distribution at $t = 0$, and σ_0 is the initial standard deviation of the distribution.

$$\frac{dR_i}{dt} = \frac{XY}{X+YR_i^2}\frac{K}{R_i^2}\exp\left(\frac{-E_{tot}}{kT}\right)\left[\exp\left(\frac{\Delta\mu(R^*(R_1, \cdots, R_N))}{kT}\right) - \exp\left(\frac{\Delta\mu(R_i)}{kT}\right)\right] \quad \forall i \in [1, \cdots, N] \quad (2)$$

The average particle radius over time at a given radius $\overline{R}_{OR}(t, T)$, which is the quantity we are able to experimentally measure via SAXS spherical diameter estimates, is computed by integrating the ODEs in eq 2. More specifically, given the solution vector $R_i(t)$, $i \in [1, \cdots, N]$ to the OR simulation, average radius prediction under OR kinetics at a given temperature, $\overline{R}_{OR}$, can be computed using the total number of particles present in the simulation at each time point.

Under reactive conditions, ripening proceeds via detachment of a Rh atom from a nanoparticle, formation of a supported monomer stabilized by adsorbates, and subsequent surface diffusion. The total activation energy is therefore expressed as

$$E_{tot} = E^f + E^d \quad (3)$$

https://doi.org/10.1021/acscatal.6c01516
ACS Catal. 2026, 16, 10398−10410

where E^f is the formation energy of the supported Rh monomer under the prevailing gas environment, and E^d is the diffusion barrier of the monomer on the support.

The formation energy includes both the thermodynamic cost of extracting a Rh atom from the bulk reservoir and the stabilization arising from adsorbate coordination. Consequently, adsorbate chemical potentials directly modify the detachment barrier and thereby the ripening kinetics. The detailed thermodynamic definitions and reference states used to evaluate E^f are provided in the Supporting Information.

2.2. The Data-Driven Model

There are multiple mechanisms for catalyst degradation (e.g., Ostwald ripening, diffusion, and coalescence). Eq 2 provides a straightforward first-principles kinetic model for Ostwald ripening, which is used as the physics-based component of the hybrid catalyst degradation model. The kinetic model for diffusion and coalescence, as derived by Wynblatt and Gjostein,[34] is more computationally intensive to evaluate and contain numerous physical parameters that are challenging to quantify. For example, the particle migration process requires modeling of mass transport, which in turn requires metal and surface-specific diffusion coefficients. Ouyang et al.[6] also proposed a method for computing chemical potentials for reactants to induce disintegration and re-dispersion of catalysts. In this mechanism, reactants may disintegrate supported metallic nanoparticles by forming complexes with the metal and spreading (re-dispersing) onto the surface. Modeling this mechanism directly also poses challenges, as quantifying parameters such as bond energies for a given system is non-trivial and can introduce significant model uncertainties.

We propose that deviations from the Ostwald ripening kinetics—potentially due to diffusion/coalescence or disintegration/re-dispersion mechanisms—can be effectively captured as a data-driven correction term in the hybrid model given experimental observations of average particle size over time. This approach leverages experimental data to account for unmodeled phenomena without explicitly incorporating the numerical complexity of other mechanistic sintering models in simulation. Instead of using a highly flexible black-box machine learning model, such as a Gaussian process, a simple parametric model is used. This substitution requires acknowledging an assumption that the proposed parametric discrepancy model structure is correct and that the errors are mean-zero and independent and identically distributed normal. Although it is difficult to ascertain the level of bias in our proposed model form, expert prior knowledge is used in formulating the parametric discrepancy function to achieve greater confidence. Specifically, the parametric function incorporates prior knowledge regarding the impact of process decision variables (e.g., operating temperature) on the nanoparticle sintering mechanisms omitted from the physics model. This leads to the black-box functional form presented in eqs 4 and.

$$F(t,\ T;\ a,\ b,\ \gamma,\ \delta) = \frac{K(T)}{1+\exp(-(\gamma+\delta t))} \tag{4}$$

$$K(T) = a + bT \tag{5}$$

The discrepancy function $F(t, T)$ is a four-parameter logistic function that adjusts the correction applied to the OR prediction over time and temperature. The carrying capacity (i.e., supremum) $K(T) = a + bT$ sets the maximum magnitude of the correction at a given temperature and at long times, wherein a (the intercept) is the temperature-independent component and b (the slope) captures how the total discrepancy evolves with temperature. Together, γ and δ govern the temporal component of the correction function. The parameter δ controls the steepness of the transition, while γ shifts the inflection point. With this logistic discrepancy function form, we encode that at early times in sintering, the contribution from the discrepancy function is small, and the hybrid model is dominated by the OR kinetics, while at later times, the correction saturates at $K(T)$, and the predicted radius asymptotes. The parameters (a, b, γ, δ) are the uncertain calibration parameters, which will be calibrated during model training to improve the fit to observed average particle radius. Thus, the black-box function $F(\cdot)$ corrects for time and temperature dependencies of the residuals between the SAXS observations of average particle size and the physics-based kinetic OR model. The carrying capacity function $K(T)$ encodes prior knowledge regarding the system, namely, that it is hypothesized that the operating temperature of the RWGS reaction will dictate the final average particle size, $\bar{R}(t_f, T)$, where t_f is the final time point of the simulated and observed RWGS reaction at a given temperature T. In other words, it is postulated, via the functional form of $K(T)$, that there is an asymptote of average particle radius under constant temperature RWGS conditions, and that the asymptote is itself a function of temperature. One possible explanation for the asymptotic or slowing of sintering over time at a fixed temperature could be the decrease in driving force as particles coarsen because the chemical potential goes by a factor of $1/R$. Another mechanistic explanation could be from strong metal−support interactions suppressing transport of particles across the surface. However, the present work cannot distinguish between these mechanisms, and we reserve that assessment for future experimental and theoretical study. For the functional form of $K(T)$, we choose a linear function of temperature in parameters a and b for simplicity and to limit the chance of over-fitting. More complicated functional forms, such as higher-order polynomials, can be easily substituted for the linear model.

2.3. The Hybrid Sintering Model

Inspired by the model presented by Kennedy and O'Hagan,[26] we define a general process control-dependent Bayesian hybrid model. The two main functional components of the hybrid sintering model are a kinetic model of Ostwald ripening (Section 2.1) and a parametric data-driven discrepancy function (Section 2.2). For more detail on the Bayesian hybrid modeling approach, we refer the reader to thorough reviews on this subject in the literature.[36−38]

The final form of the proposed hybrid sintering model for predicting average nanoparticle radius $(\bar{R})$ over time is shown in eq 6.

$$\begin{aligned}\bar{R}(t,\ T;\ \mu_0,\ \sigma_0) &= \rho(T)\bar{R}_{OR}(t,\ T;\ \mu_0,\ \sigma_0) + \\ F(t,\ T;\ a,\ b,\ \gamma,\ \delta) &+ \epsilon F(t,\ T;\ a,\ b,\ \gamma,\ \delta) = \\ \frac{K(T)}{1+\exp(-(\gamma+\delta t))}K(T) &= a + bT\rho(T) = \\ \frac{\beta_0}{(1+\exp(-\beta_1(T-T_0)))}&\epsilon \sim \mathcal{N}(0,\ \sigma_\epsilon)\end{aligned} \tag{6}$$

https://doi.org/10.1021/acscatal.6c01516
ACS Catal. 2026, 16, 10398−10410

The hybrid sintering model thus includes the kinetic OR model predictions, $\bar{R}_{OR}$, data-driven corrections functions $\rho(\cdot)$ and $F(\cdot)$, and a normally distributed error term, ϵ with standard deviation σ_ϵ, to model noise in the experimental data. Here, $\mu_0 = \mu(t = 0)$ and $\sigma_0 = \sigma(t = 0)$ are the initial particle size distribution mean and standard deviation, respectively, and T is the fixed operating temperature, or "control" variable. In eq 6, the function $\rho(T)$ represents a temperature-dependent scaling, which quantifies confidence in the correctness of the OR simulation model predictions of $\bar{R}_{OR}(\cdot)$. This scaling function is defined by calibration parameters β_0, β_1, and T_0 and is allowed to vary with temperature. This is because of our prior understanding that the kinetic OR model tends to over-predict the average radius of Rh−TiO_2 nanoparticles given the estimated DFT energies, and that the over-prediction increases as temperature increases. The temperature dependence of the function $\rho(T)$ permits additional flexibility for the kinetic OR model to adjust with temperature, as the parameters within the OR simulation itself are not calibrated in this study and are instead obtained from literature and DFT calculations. Thus, the complete set of eight calibration parameters that are "learned" in fitting the hybrid model are $[a, b, \gamma, \delta, \sigma_\epsilon, \beta_0, \beta_1, T_0]$. It is well known that there are issues of non-identifiability and confounding in Bayesian calibration with model discrepancy functions. This is why we restrict the discrepancy model flexibility via the specified, domain knowledge-informed parametric functions as opposed to more complex models.

3. RESULTS

3.1. DFT-Based Energetic Landscape

To compute the formation energy and mobility descriptors of surface-bound Rh species, we performed grand canonical genetic algorithm (GCGA[39]) sampling and DFT calculations on $Rh_1/TiO_2(110)$ under RWGS conditions at 300, 500, and 700 °C, where Rh_1 represents an isolated Rh adatom on the TiO_2 surface (full conditions in SI Table S1).

Figure 2 presents the ensemble-averaged surface phase diagrams obtained from GCGA sampling at three experimental temperatures. For each condition, the phase diagram is projected onto two chemical potential subspaces: ($\Delta\mu_{CO}$, $\Delta\mu_O$) and ($\Delta\mu_O$, $\Delta\mu_H$). Colored regions indicate the thermodynamically preferred surface configurations, derived from the Boltzmann-weighted ensemble of GCGA structures.[40,41] Because many substrate features (e.g., hydroxylation or additional TiO_2 adsorbates) do not alter the local coordination of the Rh single atom, the color scheme is defined based on the dominant Rh-centered adsorption motif: bluish regions correspond to configurations where the Rh atom binds both CO and H, reddish regions denote H-only adsorption, and greenish regions mark CO-only adsorption. Although the chemical potential range yielding CO-only states is narrow, small green regions appear at low $\Delta\mu_O$ in the left and middle panels.

The lower panels display representative Rh configurations—global minimum (GM) and low-energy local minima (LM1 and LM2)—sampled from the GCGA ensemble under each condition, along with their population fractions (only structures with a population greater than 1 % are shown). We note that multiple structures may share the same Rh coordination environment while differing in "substrate features," defined here as variations in the $TiO_2(110)$ support that do not modify the immediate Rh–adsorbate coordination. These include differences in surface hydroxylation or protonation, hydrogen coverage on Ti sites, and minor oxygen rearrangements generated during GCGA sampling. Configurations exhibiting an identical local Rh environment were therefore grouped into a single population.

At a lower temperature (300 °C), the experimental chemical potentials ($\Delta\mu_{CO} = -1.43$ eV, $\Delta\mu_H = -0.37$ eV, and $\Delta\mu_O = -2.93$ eV) lie near the phase boundary between co-adsorption of CO and H, and H-only adsorption, yielding coexisting multiple surface Rh species: $Rh(H)_2$ (79.2%), Rh(CO)(H) (16.0%), and Rh(CO) (2.6%). At elevated temperatures (500 and 700 °C), the corresponding chemical potentials (500 °C: $\Delta\mu_{CO} = -1.76$ eV, $\Delta\mu_H = -0.53$ eV, $\Delta\mu_O = -3.05$ eV;

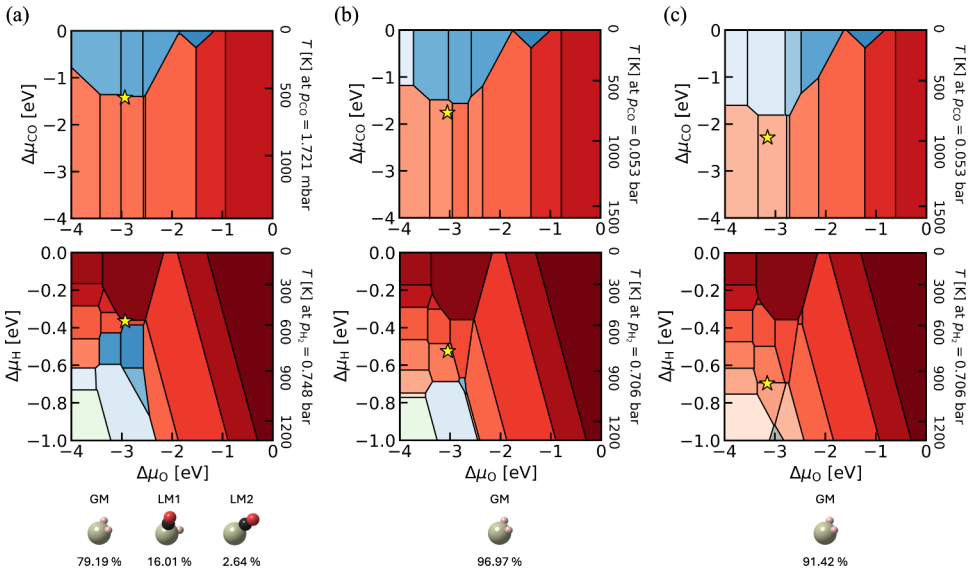

Figure 2. DFT-calculated surface phase diagrams for the $Rh_1/TiO_2(110)$ system under reverse water−gas shift (RWGS) conditions at (a) 300 °C, (b) 500 °C, and (c) 700 °C (left to right). Phase stability is projected onto two chemical potential subspaces, with yellow stars marking the experimental conditions. Colored regions denote dominant Rh-centered adsorbate configurations identified from GCGA sampling. Representative Rh structures and their population fractions are shown below in each diagram.

https://doi.org/10.1021/acscatal.6c01516
ACS Catal. 2026, 16, 10398−10410

700° C: $\Delta\mu_{CO} = -2.29$ eV, $\Delta\mu_{H} = -0.70$ eV, $\Delta\mu_{O} = -3.15$ eV) fall well within the red region, where H-only adsorption ($Rh(H)_2$) dominates (500 °C: 97.0 %, 700 °C: 91.4 %). Interestingly, these trends are consistent with the experimental CO-DRIFTS observations,[4] where gem-dicarbonyl Rh-CO species diminish at elevated temperatures and isolated Rh species dominate under RWGS conditions. Additionally, we note that Rh dicarbonyl species were not observed in our GCGA sampling, suggesting that such configurations may only be stabilized under milder conditions below 300 °C, or that they are kinetically trapped on the surface.

To quantify the thermodynamic cost of creating a mobile Rh monomer on the $TiO_2(110)$ surface under the presence of surface adsorbates, we compute the formation energy E_{ad}^{f}, following eq 3. This is defined as the sum of the bare formation energy E^{f} and the Gibbs free energy contribution of the adsorbates, as shown in SI eq 1. Using the ensemble of GCGA-identified structures weighted by their Boltzmann populations, we obtain ensemble-averaged E_{ad}^{f} values of 2.23, 2.67, and 2.67 eV at 300, 500, and 700 °C, respectively. These values serve as key inputs to the total activation energy for Ostwald ripening.

To estimate the effective diffusion barrier of Rh monomers on the $TiO_2(110)$ surface, we constructed potential energy surface (PES) maps based on DFT calculations, as shown in Figure 3. The PES does not exhibit the ideal symmetry of the stoichiometric $TiO_2(110)$ surface because the underlying reference configurations include substrate hydrogen adsorptions identified from GCGA sampling. These species locally break the intrinsic mirror symmetry of the clean support and therefore give rise to asymmetric diffusion landscapes. Full computational details of the PES construction—including grid definition, constrained relaxations, Gaussian-process interpolation, basin connectivity, and population-weighted averaging—are provided in SI Section 1.

Population-weighted effective diffusion barriers derived from the PES analysis are 0.36, 0.33, and 0.32 eV at 300, 500, and 700 °C, respectively. Here, the reported values correspond to thermally weighted effective activation energies obtained from basin-resolved hopping statistics rather than single minimum saddle barriers (see Supporting Information).

These results indicate relatively facile Rh migration even under adsorbate-modified surface conditions. At elevated temperatures, reduced adsorbate stabilization increases the monomer formation energy through changes in gas-phase chemical potentials, while enhanced thermal activation simultaneously lowers the effective diffusion barrier. This competition between detachment thermodynamics and surface mobility governs the overall sintering kinetics.

At the nanoparticle level, curvature increases the chemical potential of Rh atoms and provides the thermodynamic driving force for Ostwald ripening. Within the Gibbs–Thomson framework adopted in this work, the size-dependent nanoparticle chemical potential is expressed as

$$\Delta\mu_{NP}(R) = \frac{2\Omega\gamma_{eff}}{R} \tag{7}$$

where R is the particle curvature radius, Ω is the atomic volume of Rh, and γ_{eff} is an effective surface free energy of the supported particle.

Using $\Omega = 14.38$ Å^3/atom[6] and the DFT-derived Rh/$TiO_2(110)$ interface energy $\gamma_{ms} = 0.182$ eV/Å^2, we obtain an effective surface energy of $\gamma_{eff} = 0.197$ eV/Å^2, corresponding to a Gibbs–Thomson numerator of $2\Omega\gamma_{eff} = 5.667$ eV·Å (Figure 4). The associated Young's contact angle is $\alpha \approx 120.5°$, indicating partial wetting of Rh on $TiO_2(110)$. Details of the geometric mapping and evaluation of γ_{eff} are provided in the Supporting Information.

The corresponding adhesion energy is evaluated using the thermodynamic relation $E_{adh} = \gamma_m + \gamma_s - \gamma_{ms}$. Using our DFT-derived surface and interface energies, we obtain $E_{adh} = 1.62$ J/m^2 for the Rh/$TiO_2(110)$ interface. This value falls within the range of experimentally measured adhesion energies for late transition metals on oxide surfaces, such as 1.64 J/m^2 for Ag/$TiO_2(100)$ and 2.5 J/m^2 for Cu/$TiO_2(100)$, and the overall experimental range of ~0 to 4 J/m^2.[42] This level of agreement indicates that the present DFT description captures the correct order of magnitude of metal–oxide interfacial energetics.

In this formulation, metal–support adhesion enters explicitly into γ_{eff} through the generalized interfacial term ($\gamma_{ms} - \gamma_s$), which can be related to an adhesion energy expression via ($\gamma_m - E_{adh}$) under the standard thermodynamic definition of adhesion energy. This representation clarifies that adhesion contributes to an effective reduction in the metal surface energy and thereby modifies the curvature-driven chemical potential,[42] while γ_{eff} itself remains geometry- and facet-dependent. This relation reflects a thermodynamic energy decomposition and does not imply that γ_{eff} follows simplified isotropic geometric

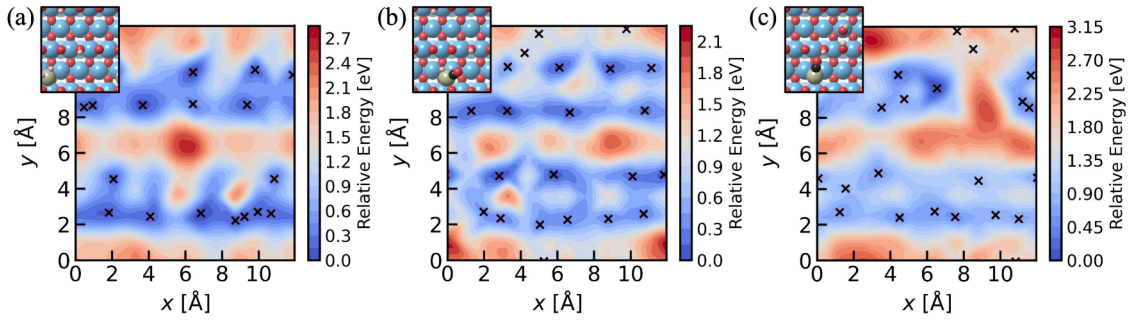

Figure 3. DFT-derived potential energy surface (PES) maps for single Rh atom diffusion on the $TiO_2(110)$ surface under representative RWGS conditions. Panels (a)–(c) correspond to the global minimum configurations with co-adsorbed H + H, CO + H, and CO, respectively, as identified from GCGA sampling (shown as insets). The heatmaps show interpolated relative energies across the surface plane, with black crosses indicating local minima used for interpolation. Color bars represent energy differences (eV) relative to the most stable adsorption site for each configuration.

https://doi.org/10.1021/acscatal.6c01516
ACS Catal. 2026, 16, 10398–10410

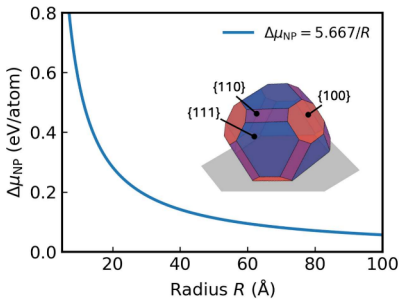

Figure 4. Size-dependent chemical potential of supported Rh nanoparticles used in the Ostwald-ripening kinetics. The solid line shows the curvature–adhesion relation $\Delta\mu_{NP}(R) = 2\Omega\gamma_{eff}/R$, with $2\Omega\gamma_{eff} = 5.667$ eV·Å per atom and R is the effective curvature radius. The schematic inset depicts the Winterbottom morphology of Rh on $TiO_2(110)$, highlighting the exposed {100}, {110}, and {111} facets and the preferred $Rh(111)/TiO_2(110)$ interface. The supported particle is mapped onto an equivalent spherical-cap geometry to express $\Delta\mu_{NP}$ as an explicit function of R (see Supporting Information).

relations. Consequently, smaller particles exhibit an elevated chemical potential and are thermodynamically biased toward Rh loss, whereas larger particles are favored to grow.

It is important to note that the γ_{eff} defined here is not equivalent to the isotropic effective surface energy obtained in the simplified hemispherical-cap limit. Instead, it represents a generalized quantity derived from facet-resolved Winterbottom constructions combined with spherical-cap geometric mapping. Consequently, γ_{eff} in the present formulation is not expected to satisfy simplified relations such as $2\gamma_{eff} = 3\gamma_m - E_{adh}$, which assume isotropic surface energies and hemispherical particle geometry.

The continuum capillarity description underlying eq 7 is applicable to nanoparticles sufficiently large to possess a well-defined average curvature and facet character. It is not intended to describe isolated atoms or sub-nanometer clusters, for which discrete electronic and structural effects dominate. For particles below a few nanometers, surface energies and adhesion may become size-dependent.[42] Nevertheless, within the nanometer-scale regime relevant to the present simulations, the curvature–adhesion formulation provides a physically consistent description of the thermodynamic driving force for ripening.

3.2. Kinetic Simulation

We simulate Ostwald ripening kinetics using the DFT-derived energetic descriptors summarized in Section . The total activation energy E_{tot} in eq 3 incorporates the ensemble-averaged monomer formation energies, population-weighted diffusion barriers, and the size-dependent nanoparticle chemical potential $\Delta\mu_{NP}(R)$. Tabulated values used in the simulations are provided in SI Section 4 (SI Table S3); computational settings and derivations are detailed in SI Section 1.

Figure 5a provides an example of how Rh–TiO_2 nanoparticle radii evolve over time under simulated OR sintering kinetics using the DFT-estimated energies. Figure 5b shows the initial (blue) and final (red) distributions of nanoparticle sizes after the simulation. Over the course of the simulation, nanoparticle count decreases as individual Rh clusters disappear due to mass transfer. This also impacts the particle size distribution, which becomes broader and shifts to the right as average particle size increases. The kernel density estimate of the population at the final time shows moderate bimodality, which indicates that while some probability density remains near the initial mean, most of the particles have grown in size during sintering via Ostwald ripening. Additional implementation details for generating the OR kinetic model data used in training the hybrid model are provided in SI Section 5.

3.3. Small-Angle X-ray Scattering Experiments

The synthesis of Rh on the TiO_2 catalyst used in the present study is reported in previous work, which can be reviewed for additional details.[43] Briefly, 0.5% of Rh species was deposited onto rutile TiO_2 nanoparticles via wetness impregnation. For in situ SAXS experiments, around 1.0 mg of pressed and sieved catalyst was packed on the Co-ACCESS flow-cell reactor. The catalyst was first pretreated by ramping temperature to 400 °C at a rate of 10 °C/min in 20 sccm of 20% O_2 in He and dwelling for half an hour. After cooling and purging by He, temperature was ramped up to 300/500/700 °C at a rate of 10 °C/min reaction mixture (24 sccm of H_2 and 8 sccm of CO_2) and dwelling for up to 6 h. The temperature range studied in SAXS was chosen to be consistent with industrial RWGS catalysts.[44,45] The reported diameters from SAXS experiments are obtained by using a unified model to extract the radius of gyration, Rg. The reported diameter is an equivalent-sphere diameter by multiplying Rg by a factor of 2 (5/3), assuming

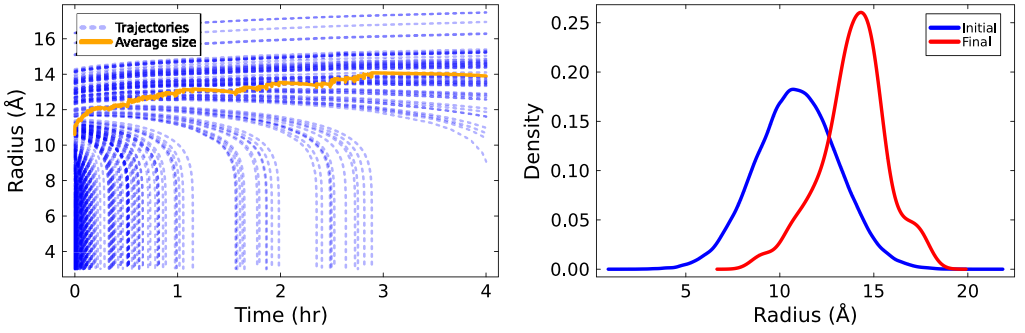

(a) (b)

Figure 5. (a) Simulated trajectories for a population of $N = 200$ Rh–TiO_2 nanoparticles. (b) Kernel density estimates for initial and final nanoparticle size distribution for $N = 200$. (a) and (b) summarize simulated Ostwald ripening results over 4 h for initial particle size distribution $R_i(0) \sim \mathcal{N}(\mu, \sigma^2)$, with $\mu = 11.0$ Å, $\sigma = 0.2$ μ, and $T = 500$ °C.

https://doi.org/10.1021/acscatal.6c01516
ACS Catal. 2026, 16, 10398–10410

that particles are spherical. The SAXS averaged diameter should be interpreted as an intensity-weighted size, as SAXS intensity scales approximately as the square of particle volume. Therefore, the SAXS-derived average size is biased toward the larger end of the distribution. Because the SAXS-derived diameter is an intensity-weighted quantity biased toward larger particles, this may contribute to the observed discrepancy between the OR simulation and experiment. Disambiguating this effect is part of future work in understanding calibration of hybrid sintering models from multiple biased data sources. For each data set at each operating temperature, the initial average radius is different at the onset of the isothermal phase due to the varying times required to reach each specific final temperature under constant temperature ramp rate. For calibration, we use a residual-preserving synthetic reconstruction of the SAXS time series at constant temperature conditions (i.e., from the completion of the temperature ramp onward) to eliminate issues due to heterogeneous time sampling and durations across temperatures. This choice standardizes the observation process for cross-condition calibration, but it also means that the results should be interpreted as verification of the hybrid-model calibration workflow rather than a direct validation against the raw SAXS measurements. Further details regarding the generation of the synthetic experimental SAXS dataset can be found in SI Section 6.

3.4. Bayesian Hybrid Sintering Model Calibration

The *posterior predictions* for the hybrid sintering model were obtained by calibrating to synthetic SAXS data at 300 and 700 °C, while 500 °C data were reserved as an independent test set. The comparison between the prior and posterior probability distributions for all calibration parameters of the hybrid model is shown in SI Section 8 in SI Figure S3.

Posterior predictions are the model predictions obtained from the *Bayesian posterior distribution*: the probability distribution of model parameters after updating their prior probability distributions with the SAXS data. In other words, they represent the calibrated or "trained" hybrid model predictions. In the present study, all Bayesian posterior probability distributions are estimated using Hamiltonian Monte Carlo via the No U-Turn Sampler (NUTS)[46] as implemented in the Julia Turing.jl probabilistic programming library[47] with 1 chain and 10,000 samples.

Given the posterior parameter distributions obtained from calibration at 300 and 700 °C, we evaluate the hybrid sintering model at the withheld test temperature of 500 °C (Figure 6b) and at training temperatures of 300 and 700 °C (Figure 6a,c, respectively). In each figure, the solid green line shows the posterior mean prediction of the average particle radius as a function of time, and the shaded region denotes the corresponding 95% Bayesian credible interval (i.e., the range in which the model predicts the true signal is most likely to lie, given the data and the assumed model). The synthetic experimental SAXS data used for calibration or testing are shown as blue points, and the Ostwald ripening (OR) model prediction (the solution to eq 2 using DFT-computed energy parameters) is plotted as an orange curve.

From the OR simulations (orange curves), it is evident that the kinetic model systematically over-predicts the sintering rate at all three temperatures, with the discrepancy being most severe at 700 °C. In the OR model with DFT-computed energetics at 700 °C, nearly all nanoparticles are predicted to sinter within the simulation time window, with most of the growth occurring within the first half an hour. This behavior implies that an effective energetic barrier is overcome somewhere between 500 and 700 °C, leading to very rapid coarsening of the nanoparticle population in the OR model at high temperatures. However, the corresponding SAXS data show substantially slower sintering under the same conditions, indicating that the OR model, as parameterized directly from DFT, substantially overestimates the true sintering rate. This systematic over-prediction in the OR simulation may also partially originate from intrinsic DFT uncertainties. For generalized-gradient-approximation (GGA)-level calculations, adsorption and activation energies typically carry uncertainties on the order of 0.1–0.3 eV.[48,49] Given the exponential dependence of the OR rate on the total activation energy, variations within this range can lead to significantly different sintering trajectories. In principle, the predictive accuracy of the OR model could be improved by explicitly calibrating or propagating these energetic uncertainties. However, in the present work, the DFT-derived energies are treated as fixed physical inputs and are not adjusted during Bayesian inference (see SI Table S3). Consequently, any discrepancy between the OR model and the SAXS data is absorbed by the calibration parameters of the hybrid correction terms in eq 6.

In contrast, the trained hybrid model (solid green lines in Figure 6) captures almost all of the experimental SAXS data at 300 and 700 °C within the shaded 95% credible interval. Relative to the OR simulation model, the hybrid model therefore exhibits a dramatic improvement in predictive accuracy at the calibration temperatures. At the test temperature of 500 °C, however, the posterior predictive band does not capture the late-time SAXS data ($t > 0.75$ hr) as well as it does for the training temperatures: the hybrid model tends to underpredict the long-time (asymptotic) average particle radius at 500 °C. Here, we use "long-time" or "asymptotic" radius to refer to the plateau value that the average particle radius is expected to approach at long reaction times according to the sintering model, even though the SAXS measurements do not necessarily reach this plateau within the experimental window. This under-prediction at 500 °C is likely a consequence of the limited size and coverage of the calibration data set (e.g., only two training sets and one test set). The quality of the out-of-sample fit across reaction temperatures would be expected to improve with additional measurements at intermediate temperatures and with varied initial conditions.[50] Despite this limitation at the test temperature, the hybrid sintering model successfully captures the qualitatively different kinetic behaviors across the wide RWGS operating temperature range studied. Thus, the hybrid framework provides a physically informed, uncertainty-aware description of sintering kinetics in Rh–TiO_2 that could be used in future work to identify operating conditions (e.g., temperature) that mitigate sintering in RWGS.

3.5. Mechanistic Insights

We conduct a model comparison analysis to quantify how much the first-principles and data-driven components each contribute to predictive performance in the hybrid nanoparticle sintering model for the Rh–TiO_2 RWGS system. This study quantifies the predictive contribution of the OR-based model relative to a structured discrepancy term, i.e., how much systematic mismatch remains after accounting for OR kinetics under the fixed energetic parameterization used here.

https://doi.org/10.1021/acscatal.6c01516
ACS Catal. 2026, 16, 10398−10410

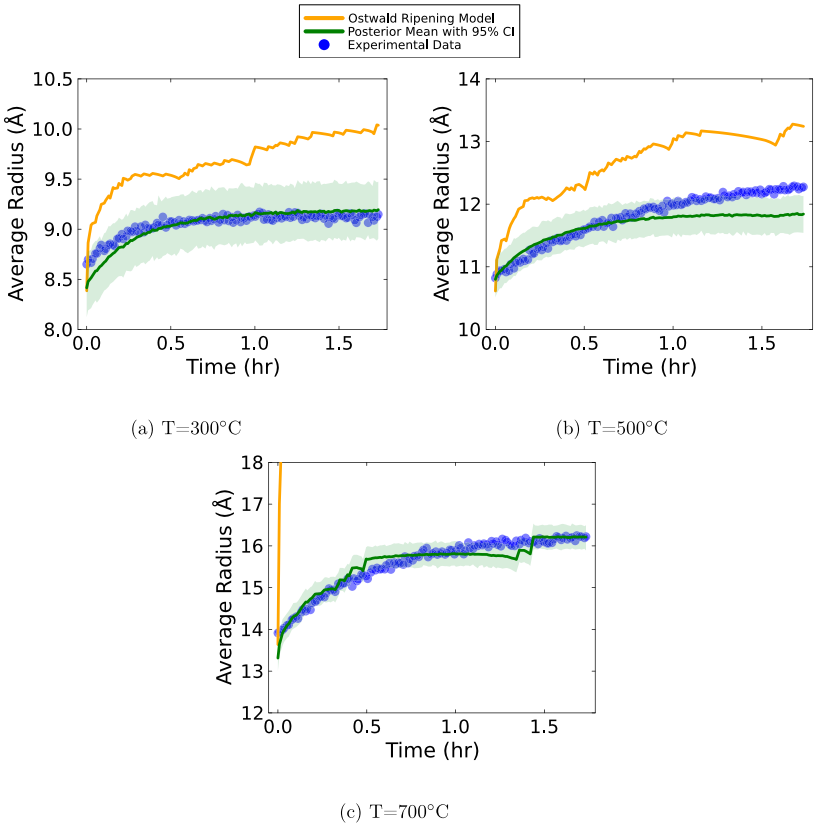

Figure 6. Posterior mean of average radius and estimated 95% confidence intervals (shaded region) over RWGS reaction time for the hybrid sintering model at (a) 300 °C, (b) 500 °C, and (c) 700 °C compared to synthetic experimental SAXS data in blue and the OR model predictions in orange.

Three model variants were constructed: (1) a physics-based model, consisting of the Ostwald ripening kinetic simulation with a temperature-dependent correction function,

$$\bar{R} = \rho(T)\bar{R}_{OR}(\mu_0,\ \sigma_0,\ T,\ t) + \epsilon$$

(2) a purely data-driven model, in which the average nanoparticle catalyst radius is described by a sigmoidal growth law,

$$\bar{R} = \frac{K(T)}{1+\exp(-(\gamma+\delta t))} + \epsilon$$

and (3) the hybrid sintering model, as shown in eq 6, which combines the physics-based OR prediction with the sigmoidal data-driven correction function. For convenience, these three models are referred to as (OR), (DD), and (ORM + DD), respectively. Here, (DD) and the additive term in (OR + DD) are used as structured model-discrepancy representations and are not intended to uniquely correspond to a single physical sintering pathway. In all of the aforementioned models, ϵ is defined as in eq 6.

Each model was trained on the same synthetic experimental SAXS datasets collected at 300 and 700 °C using Bayesian inference to obtain posterior parameter distributions for β_0, β_1, T_0, σ_ϵ in (OR), a, b, γ, δ, σ_ϵ for (DD), and β_0, β_1, T_0, a, b, γ, δ, σ_ϵ in (OR + DD). Predictive performance was then evaluated on the held-out 500 °C test dataset using the average negative log predictive density (NLPD) computed from posterior predictive samples. The NLPD is a statistical measure used to quantify the predictive performance of probabilistic models and is widely used in Bayesian model comparison.[51] Models that assign high probability to the observed values receive low NLPD scores, whereas models that place little probability mass near the observations receive high NLPD scores. Thus, lower NLPD values correspond to better predictive performance. Also, we note that because the NLPD integrates over the posterior distribution, NLPD automatically accounts for parameter uncertainty and implicitly penalizes over-fitting, tending to favor models that make accurate yet appropriately uncertain predictions. This is why we compare NLPD between models even though the models differ in total calibration parameter count. Importantly, our interpretation of the comparison presented here treats the improvements in held-out predictive performance as evidence of model inadequacy of the physics-only model hypothesis under the current DFT parameterization, not as definitive identification of a specific additional mechanism.

The average NLPD values for (OR), (DD), and (OR + DD) are shown in Figure 7. In Figure 7, each point at 300, 500, and 700 °C corresponds to the mean NLPD for a given model, and the error bars denote 95% uncertainty intervals (estimated from the posterior predictive samples). In this graphical representation, the model with the lowest value (lowest NLPD) is the model that provides the best probabilistic predictions on the sintering data.

At 300 and 500 °C, the hybrid model (OR + DD) achieves lower NLPD than both the pure physics (OR) and pure

https://doi.org/10.1021/acscatal.6c01516
ACS Catal. 2026, 16, 10398−10410

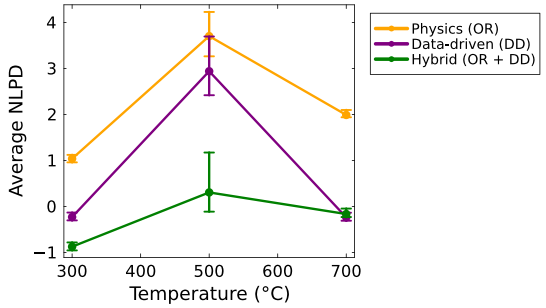

Figure 7. Average NLPD for each posterior model at different temperatures. Lower average NLPD values indicate better predictive accuracy.

data-driven models (DD), indicating superior predictive performance on both the training and the held-out data. At 700 °C, the (OR + DD) and (DD) models yield similar NLPD with overlapping uncertainty intervals, making their predictive performances statistically indistinguishable at this temperature. Overall, these results suggest that the hybrid sintering model (OR + DD) has better out-of-sample predictive accuracy than either the physics-only (OR) or data-driven (DD) model when information from multiple temperatures is considered.

The temperature dependence of the model comparison indicates that the physics-only OR model with fixed DFT energetics becomes increasingly inadequate as temperature increases. At 700 °C, a discrepancy-only representation (DD) predicts nearly as well as (OR + DD), while the OR component provides limited additional out-of-sample benefits. This pattern is consistent with multiple explanations, including temperature-dependent bias in the energetic parameterization (e.g., DFT error) or additional sintering pathways (e.g., coalescence) that are not represented in the physics-only OR model. Accordingly, we interpret the reduced incremental value of the OR component at high temperature as evidence for increasing model discrepancy, as opposed to identifying a specific alternative mechanism.

These observations can find support in recent work by Schroeder et al.[43] wherein sintering behavior of Rh−TiO_2 catalysts was measured under RWGS at 500 °C as a function of time, and Rh particle size and Rh surface concentration data lead to the hypothesis that coalescence—not Ostwald ripening—was likely the primary Rh sintering mechanism. This result is consistent with our finding that OR-only predictions require larger corrections at elevated temperatures. However, our model comparison alone does not uniquely resolve the underlying origin of the discrepancy. As noted previously, it is important to acknowledge that because the DFT energies in the OR simulation terms within the (OR + DD) and (OR) models are treated as "known," the discrepancy functions must capture both the deficiencies of the OR mechanistic model as well as any bias induced by DFT uncertainty. Therefore, mechanistic interpretations based on the hybrid model presented here are conditional on the chosen DFT parameterization. Finally, we note that the hybrid sintering model (OR + DD) involves a greater number of calibration parameters than the other two model alternatives, which may also contribute to its improved performance at lower temperatures. Disambiguating the effects of model complexity and parameterizations from the mechanistic contributions will be the focus of future work. However, the present analysis demonstrates how Bayesian model comparison can be used to systematically isolate and compare the predictive skill of different model components, thereby supporting mechanistic hypotheses about the relative importance of competing sintering pathways in a hybrid model.

Finally, we examine the temperature-dependent correction function applied to the Ostwald ripening simulation, $\rho(T)$. This function depends on the calibrated parameters β_0, β_1, and T_0, which are inferred with uncertainty in our Bayesian framework. As a result, $\rho(T)$ is itself a probabilistic, temperature-dependent function. By analyzing $\rho(T)$, we quantify how strongly the OR-based model must be rescaled as a function of temperature to remain consistent with the SAXS kinetics under the assumed DFT parameterization. In this analysis, we refrain from any effort to interpret the posterior values of the discrepancy function parameters $[a, b, \gamma, \delta]$, as the discrepancy function term is designed to absorb the aggregate of all model-data mismatch (e.g., DFT error, missing mechanisms). Therefore, any effort to assign precise mechanistic meaning to any single posterior parameter distribution is ambiguous. We focus instead on the mechanistic OR model-linked parameters $[\beta_0, \beta_1, T_0]$. Pairwise marginal posterior probability distributions are shown in SI Figure S4 and reveal significant negative correlations between the mechanistic parameters β_0 and β_1, which is expected given the functional form of $\rho(T)$ and the trade-off between logistic function-carrying capacity and transition steepness. Despite these correlations, the resulting posterior predictive intervals for the average particle radius remain narrow (Figure 6), indicating that the model predictions are robust even where individual parameters are not independently constrained or identifiable.

We compute *posterior predictive distributions* for $\rho(T)$ under both the physics-only Ostwald ripening model, (OR), and the hybrid model, (OR + DD), by sampling from the respective posterior distributions of β_0, β_1, and T_0. Here, the posterior predictive distribution for $\rho(T)$ at a given temperature is the distribution of possible correction values implied by the calibrated (trained) model after seeing the SAXS data. In practice, we can approximate this distribution by repeatedly sampling parameter sets (β_0, β_1, T_0) from the posteriors, evaluating $\rho(T)$ for each sample and then summarizing the resulting ensemble of $\rho(T)$ values via a mean and credible intervals. We denote the resulting temperature-dependent correction functions as $\rho^{OR}(T)$ for the physics-only model and $\rho^{hybrid}(T)$ for the hybrid model. The posterior means and 95% Bayesian credible intervals for $\rho^{OR}(T)$ and $\rho^{hybrid}(T)$ over the experimental temperature range are provided in Figure 8a,b, respectively.

We note that the two models exhibit qualitatively different temperature trends. In the physics-only case, $\rho^{OR}(T)$ decreases by approximately 38% as T increases from 300 to 700°. This indicates that, under the present baseline OR model parameterization, the OR simulation must be increasingly down-weighted at higher temperatures to avoid systematic over-prediction of the observed sintering kinetics. In contrast, $\rho^{hybrid}(T)$ is much smaller in absolute magnitude—roughly two orders of magnitude smaller than $\rho^{OR}(T)$ within the same temperature range—and shows only a slight increase with temperature. The narrower credible intervals for $\rho^{OR}(T)$ reflect the fact that, in the physics-only model, this single function is the primary lever available to correct temperature-dependent bias in the OR simulation. In the hybrid model, $\rho^{hybrid}(T)$ and the data-driven term jointly explain the data, leading to a better overall fit but wider marginal uncertainty in each component due to posterior trade-offs and correlations.

https://doi.org/10.1021/acscatal.6c01516
ACS Catal. 2026, 16, 10398−10410

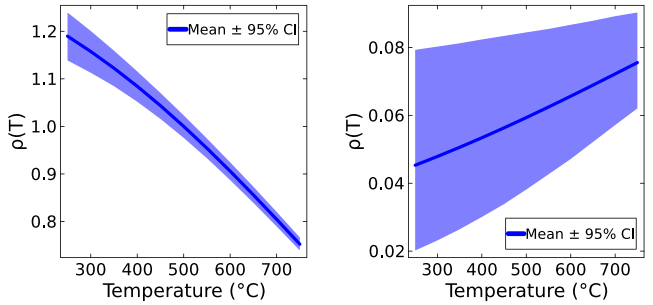

(a) Physics-only model (OR) (b) Hybrid model (OR + DD)

Figure 8. Posterior predictive mean and estimated 95% confidence intervals for the $\rho(T)$ function across temperatures in the (a) physics-only and (b) hybrid models.

From a modeling perspective, these trends indicate that in the hybrid-model formulation, the OR component contributes primarily through modest temperature-dependent rescaling via $\rho^{\text{hybrid}}(T)$, while the additive term in the discrepancy function, $K(T) = a + bT$, captures the dominant temperature-dependent residual structure required to match the SAXS observations. This can be interpreted as evidence that the physics-only (OR-only) hypothesis with a fixed DFT energy parameterization is insufficient to explain the observed sintering behavior, especially at higher temperatures. The residual error captured by the discrepancy function terms may reflect bias in the DFT calculations or additional, unmodeled sintering pathways, such as coalescence or surface interactions.

More broadly, this work provides a quantitative framework for connecting simulated sintering kinetics to experimental SAXS measurements while explicitly quantifying temperature-dependent model discrepancy and predictive uncertainties. The hybrid Bayesian formulation allows us to treat mechanistic models as testable hypotheses that can be evaluated with data and combined with data-driven components when important physics is missing or needs to be adjusted. In practical terms, the resulting hybrid sintering model delivers temperature- and time-resolved predictions of Rh–TiO_2 particle growth, with quantified uncertainty, that can be used to identify RWGS operating regimes that mitigate sintering.

4. CONCLUSIONS

In this work, we propose a hybrid model of nanoparticle catalyst sintering that combines a first-principles differential Ostwald Ripening simulation with a parametric data-driven discrepancy model. The data-driven component acts as a correction for the mechanistic model, given that (1) additional prospective sintering phenomena are not captured by the Ostwald ripening model and (2) the mechanistic Ostwald ripening model itself can present inaccuracies such as simplifying assumptions and empirically estimated energetic parameters from DFT calculations. The hybrid sintering model was trained with SAXS data of average Rh–TiO_2 nanoparticle radius over time, collected at three different reaction temperatures. Model calibration was performed using Bayesian inference, which allows for combined parameter estimation and uncertainty quantification. Prediction results for the test set show good agreement with the data at early times, with deviations at later stages of the sintering process. In particular, the hybrid sintering model appears to level out near a maximum average particle radius earlier on than the experimental test data. We would expect that access to additional datasets at other temperatures would improve the model generalization to unseen data. Importantly, analysis of an average predictive error score across the three temperatures confirmed that the hybrid sintering model provides the most accurate and well-calibrated probabilistic predictions when compared to both physics-only Ostwald ripening simulation model and purely data-driven model alternatives. Additionally, the posterior values of the kinetic Ostwald ripening simulation model scaling correction function $\rho(\cdot)$ in the hybrid sintering model are small across the studied temperatures, suggesting that a minimal adjustment of the OR model predictions is required under the fixed DFT energy parameterization. Furthermore, the predictive accuracy, as measured by the average negative log predictive density, shows that at higher temperatures (700 °C), the difference in performance between the hybrid and purely data-driven models is marginal. This indicates that, at high temperatures, the physics-only OR model hypothesis with the fixed DFT parameterization is increasingly insufficient at explaining the observed SAXS data. This discrepancy could stem from the DFT uncertainties or model inadequacy (e.g., unmodeled mechanisms). Consistent with this interpretation, recent experimental studies on Rh–TiO_2 catalysts under similar RWGS conditions have hypothesized that the mechanism of coalescence is most likely the source particle sintering. However, we note that the presented data and model comparisons do not uniquely identify the physical origin of the discrepancy. Future work will therefore focus on explicitly incorporating additional mechanisms and observables to better constrain both the energetics and mechanistic identifiability. Overall, this work demonstrates that Bayesian hybrid models combining first-principles and data-driven elements can do more than simply improve fit to data: with DFT energetics and in situ SAXS data, they provide a framework for testing mechanistic adequacy, quantifying model discrepancy, and producing predictive sintering models with uncertainty under experimentally relevant conditions. Our approach shows that carefully constructed hybrid models can be used to model complex sintering kinetics and also learn about the underlying mechanisms under realistic reaction conditions, to ultimately be used identify catalyst designs, as well as operating regimes, that are more resistant to deactivation via sintering.

■ ASSOCIATED CONTENT

Supporting Information

The Supporting Information is available free of charge at https://pubs.acs.org/doi/10.1021/acscatal.6c01516.

Additional DFT implementation details, additional DFT computational details, details regarding the grand canonical genetic algorithm, kinetic Ostwald ripening model parameter information, kinetic Ostwald ripening model computational implementation details, explanation of procedure to generate synthetic experimental data, details regarding prior probability distributions, prior and posterior distributions, and correlation plots (PDF)

https://doi.org/10.1021/acscatal.6c01516
ACS Catal. 2026, 16, 10398−10410

AUTHOR INFORMATION

Corresponding Author

Natalie M. Isenberg – *Pacific Northwest National Laboratory, Richland, Washington 99352, United States;* orcid.org/0000-0003-3050-1597; Email: natalie.isenberg@pnnl.gov

Authors

Yonghyuk Lee – *University of California Los Angeles, Los Angeles, California 90095, United States; Dongguk University, Seoul 04620, Republic of Korea*

Carolina Colombo Tedesco – *Carnegie Mellon University, Pittsburgh, Pennsylvania 15213, United States; Pacific Northwest National Laboratory, Richland, Washington 99352, United States*

Zhihengyu Chen – *SLAC National Accelerator Laboratory, Menlo Park, California 94025, United States;* orcid.org/0000-0001-5882-7076

Anastassia N. Alexandrova – *University of California Los Angeles, Los Angeles, California 90095, United States*

Christopher J. Tassone – *SLAC National Accelerator Laboratory, Menlo Park, California 94025, United States*

Robert Rallo – *Pacific Northwest National Laboratory, Richland, Washington 99352, United States*

Simon R. Bare – *SLAC National Accelerator Laboratory, Menlo Park, California 94025, United States*

Complete contact information is available at: https://pubs.acs.org/doi/10.1021/acscatal.6c01516

Author Contributions

[⊥]N.M.I. and Y.L. contributed equally to this work. N.M.I.: conceptualization, formal analysis, investigation, methodology, visualization, software, writing - original draft and review and editing. Y.L.: conceptualization, formal analysis, investigation, methodology, visualization, software, writing - original draft and review and editing. C.C.T.: investigation, methodology, writing - original draft and review and editing. Z.C.: data curation, formal analysis. A.N.A.: supervision, conceptualization, methodology, funding acquisition, writing - original draft and review. C.J.T.: supervision, conceptualization, methodology, funding acquisition. R.R.: supervision, conceptualization, methodology, funding acquisition, S.R.B.: supervision, funding acquisition, writing - original draft and review.

Notes

The authors declare no competing financial interest.

ACKNOWLEDGMENTS

This work is supported by the Division of Chemical Sciences, Geosciences, and Biosciences, Office of Basic Energy Sciences, US Department of Energy (DOE) as part of the Accelerate Innovations in Emerging Technologies initiative, FWP 101064. Use of the Stanford Synchrotron Radiation Lightsource, SLAC National Accelerator Laboratory, is supported by the U.S. Department of Energy, Office of Science, Office of Basic Energy Sciences under Contract No. DE-AC02-76SF00515. Y.L. gratefully acknowledges support from the Basic Science Research Program through the National Research Foundation of Korea (Grant No. RS-2026-25479147). Computational resources of NERSC are gratefully acknowledged. This paper has been cleared by PNNL for public release as PNNL-SA-216866.

REFERENCES

(1) Trimm, D. L. The formation and removal of coke from nickel catalyst. *Catal. Rev. Sci. Eng.* **1977**, *16*, 155–189.

(2) Guan, H.; Lin, J.; Qiao, B.; Miao, S.; Wang, A.-Q.; Wang, X.; Zhang, T. Enhanced performance of Rh1/TiO_2 catalyst without methanation in water-gas shift reaction. *AIChE J.* **2017**, *63*, 2081–2088.

(3) Kwak, J. H.; Kovarik, L.; Szanyi, J. CO_2 reduction on supported Ru/Al2O3 catalysts: cluster size dependence of product selectivity. *ACS Catal.* **2013**, *3*, 2449–2455.

(4) Matsubu, J. C.; Yang, V. N.; Christopher, P. Isolated metal active site concentration and stability control catalytic CO_2 reduction selectivity. *J. Am. Chem. Soc.* **2015**, *137*, 3076–3084.

(5) Tang, Y.; Asokan, C.; Xu, M.; Graham, G. W.; Pan, X.; Christopher, P.; Li, J.; Sautet, P. Rh single atoms on TiO2 dynamically respond to reaction conditions by adapting their site. *Nat. Commun.* **2019**, *10*, 4488.

(6) Ouyang, R.; Liu, J.-X.; Li, W.-X. Atomistic theory of Ostwald ripening and disintegration of supported metal particles under reaction conditions. *J. Am. Chem. Soc.* **2013**, *135*, 1760–1771.

(7) Hu, S.; Ouyang, R.; Li, W.-X. First-principles kinetics study of carbon monoxide promoted Ostwald ripening of Au particles on FeO/Pt (111). *J. Energy Chem.* **2019**, *30*, 108–113.

(8) Jak, M.; Konstapel, C.; Van Kreuningen, A.; Verhoeven, J.; Frenken, J. Scanning tunnelling microscopy study of the growth of small palladium particles on TiO2 (110). *Surf. Sci.* **2000**, *457*, 295–310.

(9) McClure, S. M.; Lundwall, M.; Goodman, D. Planar oxide supported rhodium nanoparticles as model catalysts. *Proc. Natl. Acad. Sci. U. S. A.* **2011**, *108*, 931–936.

(10) Campbell, C. T.; Parker, S. C.; Starr, D. E. The effect of size-dependent nanoparticle energetics on catalyst sintering. *Science.* **2002**, *298*, 811–814.

(11) Campbell, C. T. The Energetics of Supported Metal Nanoparticles: Relationships to Sintering Rates and Catalytic Activity. *Acc. Chem. Res.* **2013**, *46*, 1712–1719.

(12) Zandkarimi, B.; Poths, P.; Alexandrova, A. N. When Fluxionality Beats Size Selection: Acceleration of Ostwald Ripening of Sub-nano Clusters. *Angew. Chem. Int. Ed.* **2021**, *133*, 12080–12089.

(13) Hu, S.; Li, W.-X. Sabatier Principle of Metal-Support Interaction for Design of Ultrastable Metal Nanocatalysts. *Science.* **2021**, *374*, 1360–1365.

(14) Peterson, A. A. Acceleration of saddle-point searches with machine learning. *J. Chem. Phys.* **2016**, *145*, No. 074106.

(15) Shapeev, A. V. Moment tensor potentials: A class of systematically improvable interatomic potentials. *Multiscale Model. Simul.* **2016**, *14*, 1153–1173.

(16) Botu, V.; Batra, R.; Chapman, J.; Ramprasad, R. Machine learning force fields: construction, validation, and outlook. *J. Phys. Chem. C.* **2017**, *121*, 511–522.

(17) Westermayr, J.; Gastegger, M.; Menger, M. F.; Mai, S.; González, L.; Marquetand, P. Machine learning enables long time scale molecular photodynamics simulations. *Chem. Sci.* **2019**, *10*, 8100–8107.

(18) Hanif, W. H.; Gunawan, F. E. Random Forest Regression to Predict Catalyst Deactivation in Industrial Catalytic Process. *TEM J.* **2022**, 11,.

(19) Pankajakshan, P.; Sanyal, S.; de Noord, O. E.; Bhattacharya, I.; Bhattacharyya, A.; Waghmare, U. Machine learning and statistical analysis for materials science: stability and transferability of fingerprint descriptors and chemical insights. *Chem. Mater.* **2017**, *29*, 4190–4201.

(20) Bradley, W.; Kim, J.; Kilwein, Z.; Blakely, L.; Eydenberg, M.; Jalvin, J.; Laird, C.; Boukouvala, F. Perspectives on the integration between first-principles and data-driven modeling. *Comput. Chem. Eng.* **2022**, *166*, No. 107898.

(21) Farrar, E. H.; Grayson, M. N. Machine learning and semi-empirical calculations: a synergistic approach to rapid, accurate, and mechanism-based reaction barrier prediction. *Chem. Sci.* **2022**, *13*, 7594–7603.

(22) Bui, L.; Joswiak, M.; Castillo, I.; Phillips, A.; Yang, J.; Hickman, D. A hybrid modeling approach for catalyst monitoring and lifetime prediction. *ACS Eng. Au* **2021**, *2*, 17–26.

(23) Kay, H.; Vega-Ramon, F.; Gallen, R.; Stitt, E. H.; Zhang, D. Developing a Hybrid Modeling Framework for Enhanced Prediction in Chemical Reaction Kinetics. *Ind. Eng. Chem. Res.* **2025**, *64*, 16027–16038.
(24) Jorner, K.; Brinck, T.; Norrby, P.-O.; Buttar, D. Machine learning meets mechanistic modelling for accurate prediction of experimental activation energies. *Chem. Sci.* **2021**, *12*, 1163–1175.
(25) Luo, N.; Du, W.; Ye, Z.; Qian, F. Development of a hybrid model for industrial ethylene oxide reactor. *Ind. Eng. Chem. Res.* **2012**, *51*, 6926–6932.
(26) Kennedy, M. C.; O'Hagan, A. Bayesian calibration of computer models. *J. R. Statistic. Soc.: Ser. B* **2001**, *63*, 425–464.
(27) Miller, D. C.; Syamlal, M.; Mebane, D. S.; Storlie, C.; Bhattacharyya, D.; Sahinidis, N. V.; Agarwal, D.; Tong, C.; Zitney, S. E.; Sarkar, A.; et al. Carbon capture simulation initiative: a case study in multiscale modeling and new challenges. *Annu. Rev. Chem. Biomol. Eng.* **2014**, *5*, 301–323.
(28) Kalyanaraman, J.; Kawajiri, Y.; Lively, R. P.; Realff, M. J. Uncertainty quantification via Bayesian inference using sequential Monte Carlo methods for CO_2 adsorption process. *AIChE J.* **2016**, *62*, 3352–3368.
(29) Jantre, S.; Hoffman, M. J.; Urban, N. M.; Hillebrand, T.; Perego, M.; Price, S.; Jakeman, J. D. Probabilistic projections of the Amery Ice Shelf catchment, Antarctica, under conditions of high ice-shelf basal melt. *Cryosphere* **2024**, *18*, 5207–5238.
(30) Ghosh, S.; Pandita, P.; Atkinson, S.; Subber, W.; Zhang, Y.; Kumar, N. C.; Chakrabarti, S.; Wang, L. Advances in bayesian probabilistic modeling for industrial applications. *ASME J. Risk Uncertainty B.* **2020**, *6*, No. 030904.
(31) Isenberg, N. M.; Mertins, S. D.; Yoon, B.-J.; Reyes, K. G.; Urban, N. M. Identifying Bayesian optimal experiments for uncertain biochemical pathway models. *Sci. Rep.* **2024**, *14*, 15237.
(32) Urban, N. M.; Holden, P. B.; Edwards, N. R.; Sriver, R. L.; Keller, K. Historical and future learning about climate sensitivity. *Geophys. Res. Lett.* **2014**, *41*, 2543–2552.
(33) Eugene, E. A.; Jones, K. D.; Gao, X.; Wang, J.; Dowling, A. W. Learning and optimization under epistemic uncertainty with Bayesian hybrid models. *Comput. Chem. Eng.* **2023**, *179*, No. 108430.
(34) Wynblatt, P.; Gjostein, N. Supported metal crystallites. *Prog. Solid State Chem.* **1975**, *9*, 21–58.
(35) Parker, S. C.; Campbell, C. T. Kinetic model for sintering of supported metal particles with improved size-dependent energetics and applications to Au on TiO_2 (110). *Phys. Rev. B* **2007**, *75*, No. 035430.
(36) O'Hagan, A. Bayesian analysis of computer code outputs: A tutorial. *Reliabil. Eng. Syst. Safety* **2006**, *91*, 1290–1300.
(37) Baker, E.; Barbillon, P.; Fadikar, A.; Gramacy, R. B.; Herbei, R.; Higdon, D.; Huang, J.; Johnson, L. R.; Ma, P.; Mondal, A.; et al. Analyzing stochastic computer models: A review with opportunities. *Stat. Sci.* **2022**, *37*, 64–89.
(38) Sung, C.-L.; Tuo, R. A review on computer model calibration. *WIREs: Comput. Stat.* **2024**, *16*, No. e1645.
(39) Zhang, Z.; Gee, W.; Lavroff, R. H.; Alexandrova, A. N. GOCIA: A Grand Canonical Global Optimizer for Clusters, Interfaces, and Adsorbates. *Phys. Chem. Chem. Phys.* **2025**, *27*, 696–706.
(40) Zhang, Z.; Zandkarimi, B.; Alexandrova, A. N. Ensembles of Metastable States Govern Heterogeneous Catalysis on Dynamic Interfaces. *Acc. Chem. Res.* **2020**, *53*, 447–458.
(41) Zhang, Z.; Jimenez-Izal, E.; Hermans, I.; Alexandrova, A. N. Dynamic phase diagram of catalytic surface of hexagonal boron nitride under conditions of oxidative dehydrogenation of propane. *J. Phys. Chem. Lett.* **2018**, *10*, 20–25.
(42) Janulaitis, N.; Campbell, C. T. Predicting Adhesion Energies of Late Transition Metal Nanoparticles to Oxide Support Surfaces Using Oxide Reducibility and Metal Oxophilicity: Toward Predicting Catalyst Performance. *ACS Catal.* **2025**, *15*, 6874–6880.
(43) Schroeder, E. K.; Hong, S.; Chen, X.; Hoffman, A. S.; Chen, Z.; Khan, A.; Barber, G. D.; Bac, S.; Rioux, R. M.; Yang, J.; et al. Structural Evolution and Stability of Rh/TiO_2 Catalysts under CO_2 Hydrogenation Conditions: Influence of the Initial Rh Structure. *ACS Catal.* **2025**, *15*, 12133–12147.
(44) Santos, M. F.; Bresciani, A. E.; Ferreira, N. L.; Bassani, G. S.; Alves, R. M. Carbon dioxide conversion via reverse water-gas shift reaction: Reactor design. *J. Environ. Manage.* **2023**, *345*, No. 118822.
(45) Markowitsch, C.; Andritz, M.; Lindenthal, L.; Cotter, T.; Drexler, H.; Rameshan, C.; Lehner, M. Process intensification of the rWGS reaction by a perovskite-based catalyst. *Chem. Eng. J.* **2024**, *500*, No. 156577.
(46) Hoffman, M. D.; Gelman, A.; et al. The No-U-Turn sampler: adaptively setting path lengths in Hamiltonian Monte Carlo. *J. Mach. Learn. Res.* **2014**, *15*, 1593–1623.
(47) Ge, H.; Xu, K.; Ghahramani, Z. Turing: a language for flexible probabilistic inference. In *International conference on artificial intelligence and statistics*, **2018**; pp 1682–1690.
(48) Medford, A. J.; Wellendorff, J.; Vojvodic, A.; Studt, F.; Abild-Pedersen, F.; Jacobsen, K. W.; Bligaard, T.; Nørskov, J. K. Assessing the reliability of calculated catalytic ammonia synthesis rates. *Science.* **2014**, *345*, 197–200.
(49) Wellendorff, J.; Lundgaard, K. T.; Møgelhøj, A.; Petzold, V.; Landis, D. D.; Nørskov, J. K.; Bligaard, T.; Jacobsen, K. W. Density functionals for surface science: Exchange-correlation model development with Bayesian error estimation. *Phys. Rev. B.* **2012**, *85*, No. 235149.
(50) Jiscoot, N.; Uslamin, E. A.; Pidko, E. A. Model-based evaluation and data requirements for parallel kinetic experimentation and data-driven reaction identification and optimization. *Digit. Discov.* **2023**, *2*, 994–1005.
(51) Quinonero-Candela, J.; Rasmussen, C. E.; Sinz, F.; Bousquet, O.; Schölkopf, B. Evaluating predictive uncertainty challenge. In *Machine Learning Challenges Workshop*; Springer, **2005**; pp 1–27.

https://doi.org/10.1021/acscatal.6c01516
ACS Catal. 2026, 16, 10398–10410